Experimental determination of the x-ray atomic fundamental parameters of nickel

Yves Ménesguen, Marie-Christine Lépy, P. Hönicke, M. Müller, R. Unterumsberger, B. Beckhoff, J. Hoszowska, J.-Cl. Dousse, W. Blachucki, Y. Ito, et al.

Published in "Metrologia doi: 10.1088/1681-7575/aa9b12, 2017"
which should be cited to refer to this work.

Experimental determination of X-ray atomic fundamental parameters of nickel

Y. Ménesguen[1], M.-C. Lépy[1], P. Hönicke[2], M. Müller[2], R. Unterumsberger[2], B. Beckhoff[2], J. Hoszowska[3], J.-Cl. Dousse[3], W. Błachucki[3,*], Y. Ito[4], M. Yamashita[5], S. Fukushima[6]

[1]CEA, LIST, Laboratoire National Henri Becquerel (LNE-LNHB), bât 602 PC 111, CEA-Saclay, 91191 Gif-sur-Yvette , France

[2]Physikalisch-Technische Bundesanstalt (PTB), Abbestr. 2-12, 10587 Berlin, Germany

[3]Department of Physics, University of Fribourg, CH-1700, Fribourg, Switzerland

[4]ICR, Kyoto University, Gokasho, Uji, Kyoto 611-0011 Japan

[5]HIT, 3-1-12 Yukihira, Suma-ku, Kobe 654-0037, Japan

[6]Chemical Test Dept, Production Div., Kobe Material Testing Laboratory Co., Ltd, NewSBARU, 1-1-2, Koto, Kamigori, Ako-gun, Hyogo 678-1205, Japan

Abstract

X-ray atomic properties of nickel were investigated in a singular approach that combines different experimental techniques to obtain new and useful reliable values of atomic fundamental parameters for X-ray spectrometric purposes and for comparison to theoretical predictions. We determined the mass attenuation coefficients in an energy range covering the L- and K- absorption edges, the K-shell fluorescence yield and the $K\beta/K\alpha$ and $K\beta_{1,3}/K\alpha_{1,2}$ transition probability ratios. The obtained line profiles and linewidths of the $K\alpha$ and $K\beta$ transitions in Ni can be considered as the contribution of the satellite lines arising from the [KM] shake processes suggested by Deutsch et al. [1] and Ito et al. [2]. Comparison of the new data with several databases showed a good agreement but also discrepancies were found with existing tabulated values.

1 Introduction

Most of X-ray based analysis techniques rely on the atomic fundamental parameters either to calibrate instruments or to account for X-ray matter interactions. Reliable and up-to-date uncertainties on these parameters are of prime importance in making X-ray spectrometric techniques more competitive. This work took place in a renewal of interest from different groups around the world to measure these parameters with the best possible accuracy [3, 4, 5, 6, 7]. The main fundamental parameters are the

*present address: Institute of Physical Chemistry, Polish Academy of Sciences, 01-224 Warsaw, Poland

attenuation coefficients, the diagram lines' energies and the fluorescence yields. The relative intensities of the different fluorescence lines or the attenuation jump ratios at the transition edge are derived quantities that are also of common use. Several tables exist that gather these data in order to produce a comprehensive and useful set of parameters. Nevertheless, a lot of these datasets mostly rely on theoretical calculations or old measurements using obsolete techniques, poorly documented uncertainties or even extrapolations to experimental data. In a common effort to improve the quality of the X-ray fundamental quantities, the Laboratoire National Henri Becquerel (LNHB), the Physikalisch-Technische Bundesanstalt (PTB), the University of Fribourg (UNIFR) and the University of Kyoto (UNIKY) performed experiments with complementary techniques to provide a new comprehensive set of data for one selected element.

Our efforts in the present work have focused on nickel, a 3d transition metal, for which several tabulated and experimental data values exist in the literature and were used for comparison. The LNHB carried out the measurements of absolute mass attenuation coefficients using a transmission method of thin films [7]. As the photon energy decreases, the higher is the attenuation and the thinner the film has to be. For low energies, the transmission experiment was performed at PTB and the experimental curve was hooked up at higher photon energies for which absolute values of the mass attenuation coefficients are given by the LNHB approach. Moreover, PTB has experimental access to the determination of atomic fundamental parameters by employing the reference-free XRF approach [8] and used this approach to derive the K fluorescence yields as well as the $K\beta/K\alpha$ ratio. This ratio was also measured by another approach proposed by UNIFR. UNIFR recorded spectra using a high-resolution von Hamos spectrometer, that provides sufficient energy resolution to distinguish between the different contributions in the $K\alpha$ and $K\beta$ groups [9, 10, 11], and derived the $K\beta/K\alpha$ ratio to compare with PTB results. Finally, UNIKY took advantage of the high energy resolution allowed by the double-crystal wavelength-dispersive spectrometer together with several fitting approaches to assign the different contributions of the $K\alpha$ and $K\beta$ groups for their energy.

2 Determination of the mass attenuation coefficients

The mass attenuation coefficient, μ/ρ, is the parameter standing for the interaction probability of a photon beam in matter. It depends both on the material and the photon energy and includes the photo-absorption and scattering effects. The overall attenuation of a parallel and monochromatic photon beam at normal incidence to a target follows the Beer-Lambert law from which the mass attenuation coefficients can be derived:

$$\mu/\rho = \frac{-1}{\rho \times x} \times ln(\frac{I}{I_0}) \tag{1}$$

where I and I_0 are the transmitted and incident photon intensities respectively, ρ (in g.cm^{-3}) and x (in cm) are respectively the target density and thickness and μ/ρ is the energy-dependent mass attenuation coefficient (in cm^2.g^{-1}). A transmission measurement procedure using a monochromatic photon beam of low divergence is a convenient way to determine this parameter. In this approach, the final uncertainty budget is linked to the target characteristics and the photon flux intensities. In order to achieve the best possible uncertainty budget associated with the counting statistics, samples must have a thickness which satisfies: $2 \leq ln\,(I_0/I) \leq 4$ according to the criterion of Nordfors et al. [12]. In the following, the properties of the two photon beams and the characteristics of the samples used are described, then the different sources of uncertainty are assessed and finally the results are discussed.

2.1 The hard X-ray branch at SOLEIL Metrology beamline

At the SOLEIL synchrotron (France), the monochromator device is composed of a double Si(1 1 1) crystal whose Bragg angle is equipped with a rotary position encoder that requires a calibration. An accurate calibration of the energy axis of the monochromator is obtained by using several metal foils as

transmission targets and energy scanning around their absorption edges. The first derivative of these transmission measurements is used to determine the accurate absorption edge energies which are compared to the ones provided in the table from Deslattes [3], which finally allows to derive the corresponding angles using Bragg's law. The comparison with the absolute angles gives an offset that is provided to the monochromator device. The residual difference between the angular position given by the encoder and the values derived from the tabulated absorption edges is presented in [7] and is kept below 0.04%. The minimization of harmonics or stray light are managed in the same way as detailed in [7]. The contributions of the harmonics are significant below 7 keV and in these cases, a small detuning of the second monochromator crystal is necessary to reduce their total contribution to 0.1%. Stray light was tracked with Cu filters of various thicknesses. No evidence of a deviation in their normalized transmittances could be found within the limit of the detector sensitivity which would be a signature of stray light [7]. The transmission measurements are performed using a beam collimated at 2 × 2 mm^2 at normal incidence thus considering these areas representative of the average thickness of the whole target. Once the energy calibration is achieved, long scanning sequences with 50 and 5 eV steps are carried out within the entire available photon energy range, with smaller steps of 1 eV around the K absorption edge. The transmitted photon intensities are recorded by means of an AXUV:Al photodiode whose dark noise is subtracted from all acquired current values to derive an unbiased transmittance.

2.2 The X-ray beamlines at the PTB laboratory at BESSY II

Independent transmittance measurements were carried out at the laboratory of PTB at the electron storage ring BESSY II in Berlin (Germany) covering the low photon energy range extending from 390 eV to higher values. Monochromatized synchrotron radiation of high spectral purity was used for transmission measurements on three nickel foils with nominal thicknesses of 100 nm, 500 nm and 2 µm respectively. The measurements in the photon energy range between 390 eV and 1860 eV were performed at an undulator beamline equipped with a plane grating monochromator (PGM) [13]. One advantage of this beamline is the provision of high radiant power which is one to three orders of magnitude higher than the one of a typical bending magnet monochromator beamline. In addition, a slight detuning of the undulator harmonic energy against the PGM allows for an improved higher-order suppression capability in conjunction with the red shift of higher-order harmonics of the undulator. To further reduce the higher-order contributions, dedicated attenuation filters are used between the exit slit of the beamline and the focal plane. Depending on the operational parameters, stray light contributions of about 0.5 % to 1 % have to be taken into account. The uncertainty of the energy scale of the plane grating monochromator is in the 10^{-4} range. For the calibration of the energy scale of the PGM monochromator typical resonance lines of the gases Kr, Ar and Ne are used [14]. For photon energies from 1.8 keV up to 10 keV a four-crystal monochromator (FCM) beamline [15] with a spectral resolving power in the order of 10^4 and higher-order suppression capabilities in the range from 10^{-4} to 10^{-7} was used. The energy calibration for the FCM beamline is realized using the Si lattice constant and is regularly checked using the absorption edge position of a Cu foil.

At both beamlines, the transmission measurements are performed at an angle of incidence between the X-ray beam and the foil surface of 45°. The beam sizes were about 20 µm × 140 µm at the PGM and about 300 µm x 300 µm at the FCM beamline. The transmission measurements for each foil were done by varying the incident photon energy in steps of e.g. 5 eV, which were reduced in the vicinity of absorption edges. Using an ultra-high vacuum chamber developed in-house and dedicated to reference-free XRF analysis [8], both the transmission and the fluorescence experiments to determine line ratios and the K-shell fluorescence yield were performed. The chamber was equipped with both calibrated photodiodes and a silicon drift detector (SDD) to record the fluorescence radiation and can be installed as end-station at both PGM and FCM beamlines.

2.3 Characterization of samples

Accurate values of the sample characteristics are also required to derive absolute values of the atomic parameters. Nickel was studied in the form of metal foils supplied by the Goodfellow corporation [16] which were chosen with a mass purity better than 99.9 %. Measuring absolute mass attenuation coefficients requires the knowledge of the number of atoms interacting with the photon beam. To derive absolute values for the mass attenuation coefficients from Equation 1, density and thickness or mass and area must be known with the best possible uncertainty. Measuring the mass and area of the samples has the advantage to be more accurate and independent from X-ray analysis techniques. The samples were weighed with a calibrated microbalance used in a room whose ambient air hygrometry, temperature and pressure are controlled giving an absolute uncertainty of 9 µg at best. The area was measured with a vision machine consisting of a microscope with two calibrated stages and a picture analyzer and providing several magnifications which allowed an adequate enlargement necessary to follow a complicated shape with accuracy. The remaining sources of inaccuracy are the roughness and thickness homogeneity of the samples that were also evaluated. Finally, two samples of different thicknesses and having measurable transmission fluxes in the energy range from 3.75 keV up to 30 keV were chosen. Table 1 presents their characteristics as they are used in the different SOLEIL transmission experiments. The thin foils used at PTB could not be characterized in this manner as their thicknesses were too low for such a handling. Their mass per area was determined by scaling the experimental results of the transmission measurements for the product of mass attenuation coefficient and mass per unit area to the SOLEIL data in overlapping energy ranges.

N°	nominal thickness (µm)	mass (mg)	area (mm^2)	purity (%)
1	10	23.359(9)	276.34(4)	99.9
2	50	63.563(10)	154.49(6)	99.9

Table 1: Characteristics of the nickel samples at LNHB

2.4 Uncertainty budget

Equation 1 can be re-written, including a factor $k_P = 1$ which is responsible for an additional uncertainty due to the elemental purity of which is calculated as in [7]:

$$\mu/\rho = \frac{-1}{\rho \times x} \times ln(\frac{I}{I_0}) \times k_P = \frac{-A}{M} \times ln(T) \times k_P \tag{2}$$

where M is the mass of the sample in g, A its area in cm^2, T is the transmission ratio. To evaluate the uncertainty of the experimental mass attenuation coefficients, Equation 2 was derived according to all the influence quantities as mentioned in the "Guide to the expression of uncertainty in measurement" [17]. The uncertainty budget is expressed using the following formula:

$$\left(\frac{u(\mu/\rho)}{\mu/\rho}\right)^2 = \left(\frac{u(M)}{M}\right)^2 + \left(\frac{u(A)}{A}\right)^2 + \frac{\left(\frac{u(T)}{T}\right)^2}{ln(T)^2} + \left(\frac{u(k_P)}{k_P}\right)^2 \tag{3}$$

where the relative uncertainty of the transmission is estimated in the same way as in [7]. Table 2 gives the different contributions to the uncertainty budget of the mass attenuation coefficient measurements. For the mass attenuation coefficients in the soft X-ray range, the different contributions cannot be put in the form of equation 3 because mass and area were not measured. Instead, the contributions to the uncertainty budget originate from the matching of the different data sets (1.0 %), higher-order stray light contributions (1.0 %) and an additional uncertainty contribution of 1.0 % for photon energies below the Si-K edge [7].

contribution	sample 1 (%)	sample 2 (%)
mass	0.04	0.016
area	0.016	0.04
sample purity	0.28	0.56
transmission	0.4	0.4

Table 2: Uncertainty budget: relative standard uncertainties of each contributor.

2.5 Experimental results

The X-ray transmission measurement, using the procedures described in detail in [18], is a sequential method as it requires to remove the sample from the beam in order to measure the incoming beam intensity (I_0). The measurements resulted in a set of transmission data for Ni in the photon energy range from 3.75 keV to 30 keV, from which the energy dependent mass attenuation coefficient was calculated, covering the K- absorption edge (Figure 1). The experimental transmission data measured at the PTB were used to extend these results down to 390 eV. As the absolute mass per unit area of the thin foils is not known, the average areal mass was derived for each foil by comparing the determined mass attenuation coefficients in the overlapping photon energy regions (between 3.75 keV and 5 keV).

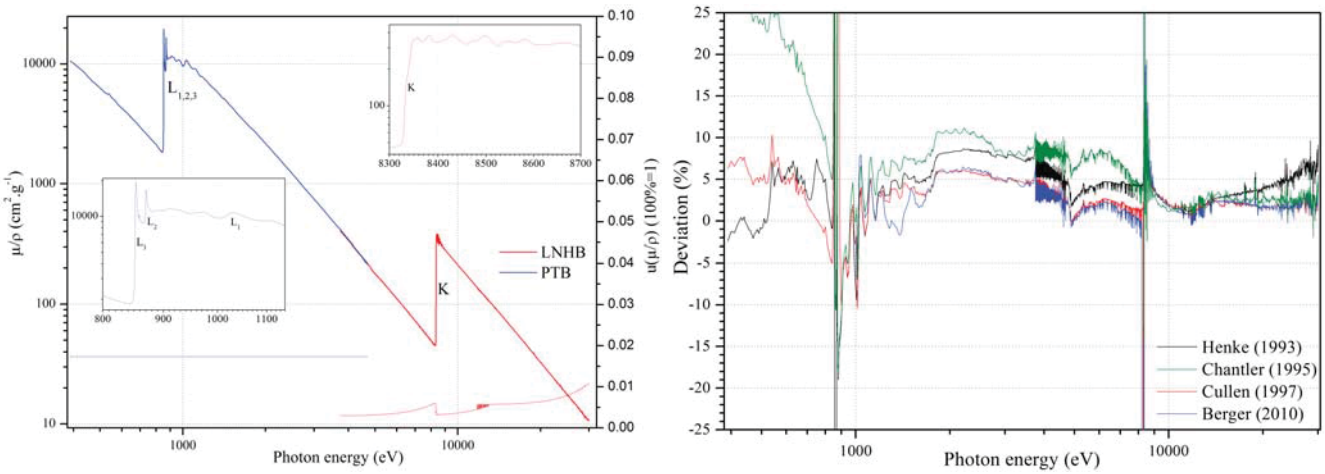

Figure 1: Left: Mass attenuation coefficients of Ni measured with an energy resolution of 1 eV around the K absorption edge (values on the left-hand vertical axis). The lower data points represent the relative standard uncertainties (right-hand vertical axis, where 0.10 means 10 %). The inset graphs are details of the mass attenuation coefficients of Ni around the K and L-absorption edges. Right: Comparison of experimental values with published databases, the relative deviation as calculated by equation 4 is plotted for the databases referenced therein.

These results were compared to theoretical or experimental values compiled in other published articles or databases such as [19, 20, 21, 22]. The relative differences between the new measurements and other tabulated values are presented in Figure 1 right. This graph plots the deviation as stated in Equation 4:

$$\frac{\Delta\mu}{\mu} = \frac{\mu_{EXP} - \mu_{DB}}{\mu_{DB}} \times 100 \tag{4}$$

where μ_{EXP} denotes for the presently measured mass attenuation coefficients and μ_{DB} stands for values from a published database. The strong relative difference found around the K and L edges are essentially due to the fine structures which are detailed in the present measurements. The $\Delta\mu/\mu$

deviation plotted for the data from Cullen [21] and Berger [22] can be as high as 6.5% in the photon energy regions between Ni L1 and K absorption edges and even higher deviations with the Henke [19] and Chantler [20] data are observed. Above the K edge, the deviation is significant between 8 and 10 keV with most databases. At higher photon energies, the behaviour of Henke values differs from the others of which no significant deviations were found. It must be noted that all the uncertainties reported by Krause et al. [23] are very high and not even known for energies below the L absorption edges of any element.

3 K fluorescence yield

The 500 nm thin foil sample used to determine for the mass attenuation coefficients was also used for the experimental determination of the K-shell fluorescence yield of Nickel. It was excited at different photon energies around the K absorption edge and for each photon energy a fluorescence spectrum was recorded by a Silicon Drift Detector (SDD). Besides these investigations, the transmission data for the photon energies of the fluorescence lines as well as for the excitation energies which were already determined for the mass attenuation coefficients were used to determine the attenuation correction factors experimentally. Thus the attenuation corrections are independent of data bases for the mass attenuation coefficient [24].

By applying Equations 5 and 6, the fluorescence production yield of each subshell can be determined,

$$\sigma_{i,shell}\left(E_0\right) = \omega_{i,shell} \times \tau_{i,shell}\left(E_0\right) = \frac{\Phi^d_{i,line}\left(E_0\right)}{\Phi_0\left(E_0\right) \times \frac{\Omega}{4\pi} \times M_{X,i}} \tag{5}$$

with $\frac{\Omega}{4\pi}$ the solid angle of detection, $\Phi_0\left(E_0\right)$ the incident photon flux, $\Phi^d_{i,line}\left(E_0\right)$ the fluorescence photon flux, and $M_{X,i}$ the attenuation correction factor given by:

$$M_{X,i} = \frac{\rho d}{\left(\frac{\mu_{s,E_0}}{sin(\Psi_{in})} + \frac{\mu_{s,E_f}}{sin(\Psi_{out})}\right)\rho d} \times \left(1 - exp\left(-\left(\frac{\mu_{s,E_0}}{sin\left(\Psi_{in}\right)} + \frac{\mu_{s,E_f}}{sin\left(\Psi_{out}\right)}\right)\rho d\right)\right) \tag{6}$$

In the case of the Ni K shell, this requires that both the fluorescence photon flux $\Phi^d_{i,line}\left(E_0\right)$ for Ni K fluorescence and the photoionization cross section of the Ni K shell $\tau_{i,shell}\left(E_0\right)$ can be derived from the experiments. The latter is also obtained from the available transmission data in the vicinity of the K absorption edge by removing the scattering contributions and splitting into photoionization contributions from the energetically lower shells and the K-shell [25]. The fluorescence photon fluxes for the Ni $K\alpha$ and Ni $K\beta$ fluorescence lines are derived from the recorded SDD spectra by deconvolution using the known detector response functions [14] for the fluorescence lines as well as relevant background contributions, e.g. bremsstrahlung. The detection efficiencies for Ni $K\alpha$ and Ni $K\beta$ fluorescence photons are known due to the use of a calibrated SDD.

	ω_K
PTB	0.410(14)
Krause (1979)	0.412(21)
Cullen (1997)	0.401

Table 3: Experimentally determined K-shell fluorescence yield of the Ni K-shell in comparison to commonly used literature values [26, 21].

The determined Ni K shell fluorescence yield is shown in Table 3 together with other commonly used literature values [26, 21]. The agreement of the new value with the literature data is very good. Moreover, the present result is characterized by a smaller uncertainy with respect to the very often

used value from Krause's value. The main contributors to the presented uncertainty budget are the attenuation correction factor and the determination of the photoelectric cross section, Table 4 lists all uncertainty contributions [27].

Origin of the contribution	relative standard uncertainty (%)
Conamination by higher harmonics of incident photons	10^{-3}
Measurement of incident photon intensity with photodiode	1
Determination of solid angle of detection	0.7
Detection efficiency of silicon drift detector	1.5
Determination of fluorescence intensities (fitting procedure)	1.5
Attenuation correction factor	2.0
Determination of photoelectric cross-section	2.0

Table 4: Experimentally determined contributions to the standard uncertainty of the fluorescence yield.

4 $K\beta/K\alpha$ transition probability ratio

4.1 SDD based measurements at PTB

Using the derived fluorescence photon fluxes obtained during the experimental determination of the K-shell fluorescence yield, the $K\beta/K\alpha$ transition probability ratio was calculated. The fluorescence photon intensities used in the transition probability ratio determination were corrected for the self-absorption effect taking place within the studied sample. The experimental transmission data acquired for the 500 nm-thick Ni foils were used and the attenuation correction factors were calulated according to Equation 6. Using this approach in combination with the known detection efficiencies for the Ni $K\alpha$ and $K\beta$ fluorescence lines, we derived a $K\beta/K\alpha$ ratio of 0.132(6).

4.2 High energy resolution measurements with the von Hamos bent crystal X-ray spectrometer at the University of Fribourg

4.2.1 Experimental setup and data analysis

The $K\beta/K\alpha$ transition probability ratio was determined from high energy resolution measurements of the Ni K X-ray spectrum performed at the University of Fribourg (UNIFR), Switzerland, using a von Hamos bent crystal X-ray spectrometer [28] and a conventional X-ray tube. The principal elements of the von Hamos X-ray spectrometer are the X-ray source, a cylindrically bent crystal, and a position-sensitive detector. The X-ray fluorescence source and the 2D position-sensitive detector are located on the axis of dispersion (crystal axis of curvature), and the cylindrically bent crystal provides focusing in the nondispersive plane. The effective or geometrical X-ray source of radiation is defined by a rectangular slit while the irradiated sample is located behind. Since the slit position is fixed while the crystal position changes with the Bragg angle, the sample is translated along the beam direction and the orientation of the slit is automatically adjusted to keep the slit width unchanged. Such a design allows the use of conventional high-power X-ray tubes for sample irradiation. The diffracted X-rays form a 2D image on the detector whose location along the dispersion axis of the detector corresponds geometrically to the energy axis of the X-ray spectrum. The CCD detector allows discrimination against higher-order crystal reflections and also a rejection of background events by setting appropriate energy windows. Depending on the Bragg angle and the crystal and detector dimensions along the dispersion direction, the von Hamos X-ray spectrometer allows collection of an X-ray spectrum over an energy bandwidth of few tens to few hundreds of eV.

For the $K\alpha$ and $K\beta$ X-ray spectra measurements of Ni the X-ray spectrometer was equipped with a Si(311) (2d =0.3275 nm) segmented type crystal [29] with a curvature radius of 25.0 cm, and a back-illuminated charged coupled device (CCD) detector consisting of 1340 columns and 400 rows with a pixel size of 20×20 μm^2 [30]. The CCD was cooled thermoelectrically to 228 K. For sample irradiation the high-power side-window Cr-anode X-ray tube was operated at 40 kV and 20 mA. A self-supported metallic foil of Ni from Goodfellow corporation [16] with a thickness of 26.18 μm and 99.99 % purity was used. To minimize self-absorption effects, the sample was tilted to a given φ corresponding to the median angle between the direction of irradiation and observation. X-ray spectra were collected in the first order of diffraction and the slit width was 0.1 mm. The resulting experimental resolving power of the X-ray spectrometer was 2.24×10^{-4}, and thus the energy resolution was comparable to the natural linewidths of the Ni K X-ray diagram transitions.

The measured $K\alpha$ ($K\alpha_{1,2} + K\alpha_{1,2}L^1$) and $K\beta$ ($K\beta_{1,3} + K\beta_{1,3}L^1 + K\beta_5$) X-ray transitions are presented in Figure 2. The spectra were fitted by means of a least squares fitting algorithm using Voigt functions.

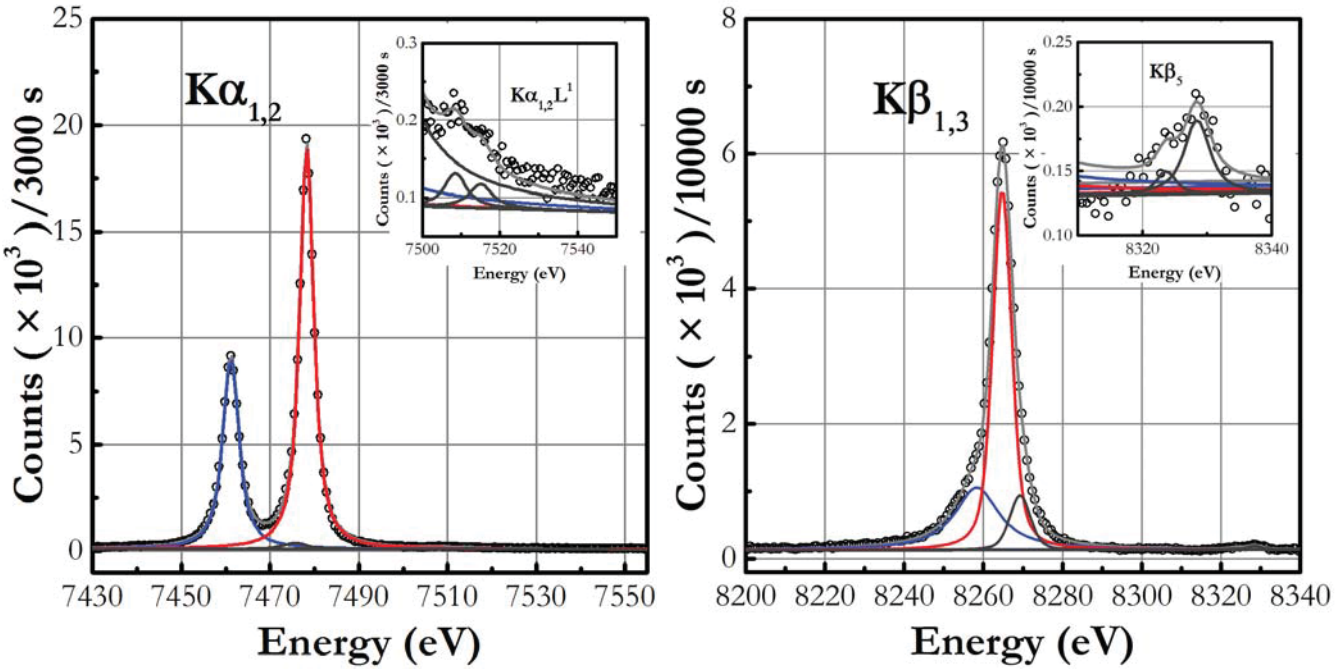

Figure 2: Left: High energy resolution K X-ray spectra of Ni showing the $K\alpha_{1,2}$ diagram lines and the first order L satellite $K\alpha_{1,2}L^1$. Right: $K\beta$ ($K\beta_{1,3} + K\beta_{1,3}L^1 + K\beta_5$) X-ray emission lines. Open circles correspond to the experimental points and the solid lines to the fitted transitions.

In order to extract the $K\beta$ to $K\alpha$ transition probabilities ratios the fitted intensities of the X-ray transitions were corrected for the relative differences in the CCD detector quantum efficiency F_{QE}, crystal reflectivity F_C, solid angle of detection F_{Ω_D} and irradiation F_{Ω_S}, effective source size F_S, and self-absorption effects in the sample F_A. The total correction factor F_{corr} reads:

$$F_{corr} = F_{QE} \times F_C \times F_{\Omega_D} \times F_{\Omega_S} \times F_S \times F_A$$

The variation of the CCD quantum efficiency as a function of the photon energy was accounted for following the formulas reported in [30] and using the mass attenuation coefficients from the XCOM database [22].The crystal peak reflectivity was calculated for each transition of interest with the XOP (X-Ray Oriented Programs) software package [31]. As the diagram K X-rays are not polarized, the average value of the crystal peak reflectivity for X-rays linearly polarized in the horizontal plane and in the vertical plane was used.

The calculation of the solid angle of detection Ω_D was based on a geometrical ray-tracing approach. In the von Hamos geometry the spectrometer Ω_D varies with the photon energy E, and can be expressed as:

$$\Omega_D(E) = \int_{-\Delta\theta_D/2}^{\Delta\theta_D/2} \int_{\alpha_{min}(E)}^{\alpha_{max}(E)} sin\vartheta d\vartheta d\varphi$$

where $\alpha_{min}(E) = [\pi - \alpha_{av}(E)]/2$, $\alpha_{max}(E) = [\pi + \alpha_{av}(E)]/2$ and $\Delta\theta_D(E)$ represents the crystal Darwin width for the photon energy E. The angle $\alpha_{av}(E)$ is defined by $\alpha_{av}(E) = 2 \times arctan[h_{av}(E)/(2 \times l(E))]$, where h_{av} represents the average height of the crystal seen by the part of the sample contributing to the production of the observed fluorescence, and the length $l(E)$ corresponds to the sample to crystal distance for a given Bragg angle $\vartheta(E)$ along the observation direction. The $\Delta\theta_D(E)$ widths, calculated with the XOP code, are weighted means of the Darwin widths for linearly polarized X-rays in the horizontal and in the vertical plane. The F_S correction factor accounts for the change of the effective area of radiation source as a function of the photon energy, namely $S_{eff}(E) = h_{eff}(E) \times w_{eff}(E)$, where $h_{eff}(E)$ is the effective height and $w_{eff}(E)$ is the effective width given by: $w_{eff}(E) = w_{slit}/sin[\vartheta(E) + \varphi(E)]$. Since in the modified von Hamos slit geometry the photon flux incident on the sample decreases quadratically with the distance separating the sample and the anode of the X-ray tube, the correction factor for the solid angle of irradiation F_{Ω_S} was determined from the known distances between the X-ray tube anode and the sample for the different X-ray emission lines.

To correct for the self-attenuation, the ratio of the real target output flux A to the flux A_0 of a hypothetical target without attenuation was computed for the $K\alpha$ and $K\beta$ X-ray line transitions with the following expression:

$$\frac{A}{A_0} = \frac{\int_0^{\rho d} \left\{ \left[\int_{E_K}^{HV} I(E) \times exp\left(-\mu(E) \times \frac{x}{cos(\varphi)}\right) \times \sigma(E)\, dE \right] \times exp\left(\mu(E_X) \times \frac{x}{sin(\vartheta+\varphi)}\right) \right\} dx}{\rho d \int_{E_K}^{HV} I(E) \times \sigma(E)\, dE}$$

where HV is the X-ray tube voltage, E_K the K-edge absorption energy, ρd the sample thickness in g.cm^{-2}, and $\mu(E_X)$ the mass attenuation coefficient in cm^2.g^{-1} for the X-ray transition energy E_X. The incident photon intensity of the X-ray tube as a function of energy $I(E)$ was simulated using the empirical formula from [32] and for the photoionization cross sections $\sigma(E)$ and mass attenuation coefficients $\mu(E)$ the values determined in this work were adopted. The total correction factor F_{corr} for the measured $K\beta$ to $K\alpha$ intensity ratio amounts to 1.096(41). Results for the different factors are presented in Table 5. Furthermore the following relative uncertainties were adopted for the different factors: 1% for the CCD detector quantum efficiency F_{QE}, 1% for the crystal reflectivity F_C, 2 % for the solid angles F_{Ω_D} and F_{Ω_S} including F_S, and 2 % for the self-absorption F_A. Finally, the contribution of the statistical uncertainty from the fitting procedure was also included in the final uncertainty budget.

F_{QE}	F_C	F_{Ω_D}	F_{Ω_S}	F_S	F_A	F_{corr}
1.157	0.957	1.158	1.020	0.910	0.921	1.096

Table 5: Total correction factor F_{corr} and the correction factors for CCD detector quantum efficiency F_{QE}, crystal reflectivity F_C, solid angle of detection F_{Ω_D}, solid angle of irradiation F_{Ω_S}, effective source size F_S, and self-attenuation F_A.

4.2.2 Results

The obtained ratios of the $K\beta$($K\beta_{1,3}$+$K\beta_{1,3}L^1$+$K\beta_5$) to $K\alpha$($K\alpha_{1,2}$+$K\alpha_{1,2}L^1$) and $K\beta_{1,3}$ to $K\alpha_{1,2}$ transition probabilities for Ni are presented in Table 6 in comparison to other experimental, semi-empirical, and theoretical data. The values obtained in this work by UNIFR, UNIKY and PTB are in excellent agreement within the quoted uncertainties. Moreover, the commonly used values of Elam [33] and CXRO [34] are

showing clear discrepancies with these new data. The advantage of the reported new data relies in its improved reliability which was achieved by validating the results with three independent measurements employing different experimental conditions and apparatus, and by using the experimentally determined new mass attenuation coefficients for the attenuation corrections.

	$K\beta/K\alpha$	$K\beta_{1,3}/K\alpha_{1,2}$
UNIFR	0.133(7)	0.129(7)
PTB	0.132(6)	
UNIKY		0.128(13)*
Hölzer [35]		0.147(5)
Ertugral [36]	0.133(3)	
Elam [33]	0.146	0.145
CXRO [34]		0.113
Schönfeld [37]	0.138(1)	
Scofield [38]	0.123	
Scofield [39]	0.140	0.136
Polasik [40]	0.136	

Table 6: Ratios of the $K\beta(K\beta_{1,3} + K\beta_{1,3}L^1 + K\beta_5)$ to $K\alpha(K\alpha_{1,2} + K\alpha_{1,2}L^1)$ and $K\beta_{1,3}$ to $K\alpha_{1,2}$ transition probabilities for Ni. For comparison other experimental and semi-empirical data and theoretical predictions are included. The present $K\beta_5$ to $K\beta_{1,3}$ intensity ratio yields 0.039(4).* See next section for explanation.

5 Energies and linewidths of $K\alpha$ and $K\beta$ transitions

For a long time, the investigation of the X-ray spectra of the 3d elements has focused on the needs in applications. It is well known that the profile of the $K\alpha_{1,2}$ and $K\beta_{1,3}$ emission lines in 3d elements have an asymmetry. Berger [41] first proposed to fit the shape of both the Cu $K\alpha_1$ and $K\alpha_2$ lines by two Lorentzians as a simple model of the analysis. Deutsch et al. gave a physical meaning to the fitting based on the theoretical consideration: the asymmetry in Cu $K\alpha$ spectra is due to a 3d spectator vacancy [1]. According to the description of the profiles by a two-Lorentzian model, Ito et al. [42] and Polasik et al. [43] investigated the emission line shapes in Ti ~ Zn elements and concluded that the FWHM of the $K\alpha_{11}$ which corresponds to $K\alpha_1$ line increases from Ti ~ Zn as compared with the semi-empirical FWHM reported by Krause and Oliver [44]. Moreover, Ito et al. [42] reported that $K\alpha_{21}$ (corresponding to $K\alpha_2$ line), shows a different aspect which may be ascribed to the L_2 – $L_3M_{4,5}$ Coster-Kronig transition. More recently Ito et al. also concluded that satellite lines arising from shake-off appear between the $K\alpha_1$ and $K\alpha_2$ emission lines and that the asymmetry index of $K\alpha_1$ in 3d elements from Sc to Zn is ascribed to the existence of a 3d spectator hole [2]. A series of K line spectra were recorded by a high-resolution double-crystal X-ray spectrometer to reconfirm the line energies, FWHM and asymmetry index of the Ni $K\alpha_{1,2}$ transitions, and confirm the line energies and FWHM of the $K\beta_{1,3}$ transitions respectively. For their multiple Lorentzian representation in 3d elements, no attempt was made to take into account the physical origin of the asymmetry of these lines. It was reported that the approach of addressing only the width and asymmetry of a line, is not convenient to account for the shapes of complex spectra such as those of the 3d transition metals [45]. Anagnostopoulos et al. [46] calculated the [1s3p] and [1s3d] shake probabilities in Sc and found 15 and 38 %, respectively. Moreover, Lowe et al. [47] calculated the shake probability of the double electrons transition in order to elucidate the [1s3d] contribution in 3d elements. The contribution of [1s3d] shake probability in Sc was estimated at almost 40 %, which is too large. More recently, Chantler et al. [5] reported that the observed Ti $K\alpha_1$ spectra had the symmetric profiles different from the results in Cu $K\alpha_{1,2}$ spectra reported by Deutsch et al. [1]. The results seem to have deepened the degree of confusion in the

research of the atomic spectra, although a broad symmetric instrumental function tends to suppress the line asymmetry and gives systematically small values for the index of asymmetry [35]. UNIKY used the two Lorentzian model for each $K\alpha_1$ and $K\alpha_2$ diagram line, as proposed by Berger, to take into consideration the shake process to systematically investigate the emission line shapes in Ni obtained by a high-resolution double crystal X-ray spectrometer.

5.1 Experimental conditions

The measured spectral distribution of an emission line differs, in general, from the true energy distribution of emitted X-rays out of the sample because of the effect due to the instrumental function of the spectrometer (spectrometer window function), in particular, source size and slit for a single crystal spectrometer. However, in the case of a double-crystal spectrometer with a higher order Bragg reflection, the instrumental function can be narrowed so that the correction for the window function remains simple (see [2, 48] for details). Hence, we used a double-crystal spectrometer system (RIGAKU 3580EKI) with an end-window type X-ray tube with a rhodium target as anode material.

The metallic foil of Ni was placed in vacuum conditions. The X-ray tube was biased at 40 kV with a current of 60 mA and both Si(220) crystals were used in symmetric reflection. The detector used was a sealed Xe gas proportional counter guaranteeing a maximum efficiency in the energy range considered. The other experimental conditions (accumulation time, angle step, repetition) for the measurements are presented in Table 7. The fluorescence X-ray spectra of both $K\alpha_{1,2}$ and $K\beta_{1,3}$ diagram lines of Ni were measured several times with an accumulation time of several seconds per angle step in order to minimize the statistical uncertainty. The observed $K\alpha_{1,2}$ and $K\beta_{1,3,5}$ emission spectra of Ni were measured using the anti-parallel double crystal X-ray spectrometer and are shown in Figure 3. Neither smoothing nor correction was applied to the raw data. The energy calibration was done using the values of Deslattes [3] for the $K\alpha_{1,2}$ diagram lines. Nevertheless, the resolution at the Ni $K\beta_{1,3}$ lines of the double-crystal X-ray spectrometer being extremely high (1.45×10^{-5}), it was possible to distinguish the satellites' structure which can not be processed even by using a more recent approximate value (Deslattes' value). Therefore, we used Bearden's value of Ni $K\beta_1$ as reference [49]. The vertical divergence slit is 0.573 degree in this spectrometer.

Line	acumulation time (s./point)	step width (degree (2θ))	repetition
$K\alpha_{1,2}$	20	0.0005	3
$K\beta_{1,3,5}$	50	0.001	3
$K\alpha_{1,2}; K\beta_{1,3}$	120	0.01	3

Table 7: Experimental conditions of the measurements using the two-crystal Si(220) X-ray spectrometer.

5.2 Results and discussion

The $K\alpha_{1,2}$ line shape in 3d elements is generally described by its FWHM and its index of asymmetry. Both values allow a comparison with other experimental results and a general classification of our measurements in relation to other reference data. However, it should be noted that the line shape cannot be described precisely by a simple asymmetric profile in all cases including $K\alpha_{1,2}$ lines as also suggested by Hölzer et al. [35]. Moreover, it is a possibility that various widths in previous measurements on 3d elements are ascribed to the incomplete correction for the instrumental broadening [35]. Therefore, in the double crystal spectrometer, simple correction can lead to a significant improvement in the result, that is, the 'true' FWHM of the emission line can be determined by a simple substraction of the crystal dispersion from the FWHM of the measured emission line [48]. Our case belongs to this approach.

The measurement of the Ni $K\alpha$ lines was performed three times using the high-resolution double-crystal X-ray spectrometer and the results in the fitting analysis are presented in Figure 3 left. Several

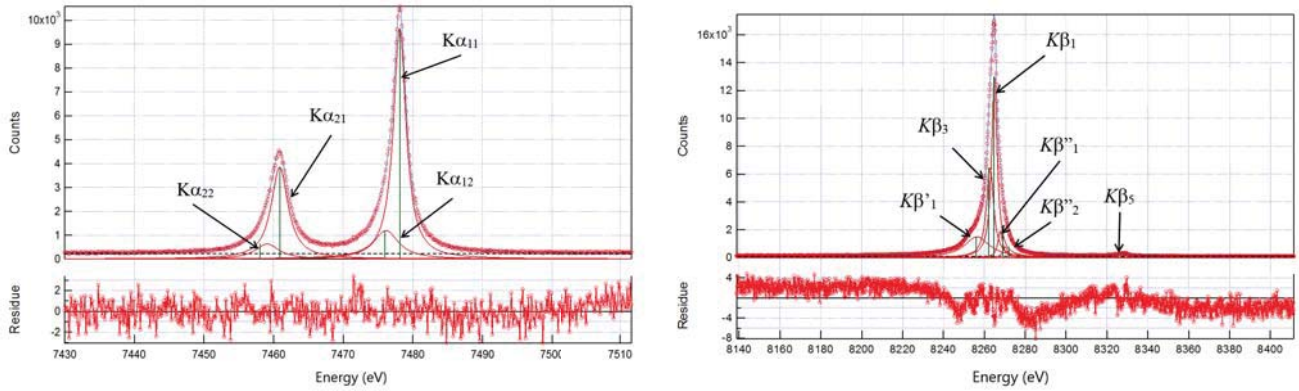

Figure 3: Left: The observed $K\alpha_{1,2}$ spectra of Ni are shown with the Lorentzian fitting model [41, 1, 42]. The usual names of $K\alpha_1$ and $K\alpha_2$ are presented here as $K\alpha_{11}$ and $K\alpha_{21}$, respectively and $K\alpha_{12}$ and $K\alpha_{22}$ are the contribution of the shake probability due to the [KM] double electron transition [2]. Right: The observed $K\beta_{1,3}$ and $K\beta_5$ spectra in elemental Ni are shown with the Lorentzian fitting model [41, 1, 42].

parameters were determined for the Ni $K\alpha_{1,2}$ diagram lines using two different approaches depending on the line shape modelling. In the first approach, we used a four Lorentzian fitting and derived the line energies, the observed FWHM, the corrected FWHM (CF), and the relative intensity ratio for each Lorentzian. These results are shown in Table 8 together with the intensity of the [KM] shake contributions ($K\alpha_{12}$ and $K\alpha_{22}$) relative to the $K\alpha_1$ diagram line and the recommended natural line widths [50]. The other model used two asymmetric Lorentzians and the fitting results are presented on Table 9 and include the line energies, the full width at half maximum (FWHM), the asymmetric index and the relative intensity ratio for each line. For Ni $K\beta_{1,3}$ (Figure 3 right), the line energies, the FWHM and the relative intensity ratio in each Lorentzian model were determined as shown in Table 8 together with the contribution of [KM] shake processes probabilities and the recommended natural line widths [50]. The Lorentzian model was used for an analytic representation of $K\beta_{1,3}$ lines [41, 1, 42]. The uncertainties reported here are only statistical resulting from the fitting processes, and the limited reproducibility of the experimental setup (~0.04 eV). To obtain realistic uncertainties, the errors originating from the energy calibration have to be considered. Absolute $K\alpha_{1,2}$ and $K\beta_{1,3}$ photon energies for all 3d elements between Cr and Cu can be found in [35].

4 symmetric Lorentzian fitting						
Line	Energy (eV)	Energy (eV)#	FWHM (eV)	CF* (eV)	natural line** (eV)	Intensity (Rel.)
$K\alpha_{11}$	7478.22(7)	7478.2521(45)	2.15(1)	2.02(1)	1.92	100.00
$K\alpha_{12}$	7476.11(5)		4.25(5)			22.4(7)
$K\alpha_{21}$	7460.99(7)	7461.0343(45)	2.84(2)	2.72(2)	2.37	51.5(7)
$K\alpha_{22}$	7459.24(8)		4.03(6)			12.4(10)

Table 8: Fitting parameters for Ni $K\alpha_{1,2}$ spectra using four symmetric Lorentzians to determine the contribution of the shake processes and deducing the natural line widths [2]. * These values are corrected based on Tochio's method [48]. **These values are the recommended natural line widths after J. L. Campbell and T. Papp [50]. # R. D. Deslattes [3].

The corrected FWHM (CF) of the $K\alpha_{11}$ (usually named $K\alpha_1$) and $K\alpha_{21}$ (usually named $K\alpha_2$) lines in Ni element are in good agreement with the recommended ones of the $K\alpha_1$ and $K\alpha_2$ emission lines reported by Krause & Oliver [44] and Campbell & Papp [50], confirming the reproducibility of these values. For the CF, we obtained each value for $K\alpha_{11}$ and $K\alpha_{21}$, or $K\beta_1$ and $K\beta_3$ diagram lines, respectively, from

2 asymmetric Lorentzian fitting				
Line	Energy (eV)	FWHM (eV)	A. I. ***	Intensity (Rel.)
$K\alpha_1$	7478.27(7)	2.64(1)	1.31(1)	100.00
$K\alpha_2$	7460.93(7)	3.20(1)	1.18(1)	51.43(7)

Table 9: Fitting parameters for Ni $K\alpha_{1,2}$ spectra using two asymmetric Lorentzians. *** A. I. means asymmetric index.

6 symmetric fitting						
Line	Energy (eV)	Energy (eV) #	FWHM (eV)	CF* (eV)	natural line** (eV)	Intensity (Rel.)
$K\beta_1$	8264.98(14)	8264.66(7)	3.09(19)	2.97(19)	2.69	100.00
$K\beta_3$	8262.90(16)	8264.66(7)	4.14(15)	4.03(15)	2.69	77.77(13.82)
$K\beta_1'$	8256.52(22)		14.86(12)			59.56(7.31)
$K\beta_1''$	8267.49(28)		2.88(51)			16.19(4.66)
$K\beta_2''$	8270.00(34)		3.08(27)			7.83(2.56)
$K\beta_5$	8327.45(24)	8328.6(3)	3.19(16)			10.23(1.06)

Table 10: Fitting parameters for Ni $K\beta_{1,3}$ spectra using 6 symmetric Lorentzians for the the contribution of the shake processes and deducing the natural line widths of $K\beta_{1,3}$ lines. * These values are corrected based on Tochio's method [48]. **These values are the semi-empirical natural line widths after M.O. Krause and J. H. Oliver [44]. *** A. I. means asymmetric index. # J. A. Bearden [49].

the observed FWHM through Tochio's method [48]. As shown in Table 8, the CF of the $K\alpha_{21}$ is about 0.7 eV larger than that of $K\alpha_{11}$ in Ni. The difference of CF in $K\alpha_1$ and $K\alpha_2$ lines is considered to be due to L_2-$L_3M_{4,5}$ Coster-Kronig transition [2]. According to the shake processes, when K shell ionization accompany additional outershell ionization or excitation as often happens, it can be considered that the $K\alpha$ X-rays are shifted in energy with respect to the diagram lines. The simultaneous ionization in the L shell leads to $K\alpha$ X-ray satellites, for example, $K\alpha_{3,4}$ satellites, easily resolved from the diagram lines using X-ray crystal spectrometer. However, when ionization occurs in the M shell, the shift in K X-ray energy is generally less than the natural line width of the diagram lines. Therefore, the diagram lines in especially 3d elements can be strongly contaminated. Two Lorentzian models for each diagram line was applied for the systematic analysis in the elements region: $K\alpha_{11}$ and $K\alpha_{21}$ are nominally $K\alpha_1$ and $K\alpha_2$, respectively. $K\alpha_{12}$ and $K\alpha_{22}$ are attributed to the [KM] shake contribution. For the same reasons the $K\beta$ lines can also and even more be contaminated compared with the satellites in the $K\alpha$ lines. The $K\beta_{1,3}$ lines are analyzed using 5 symmetric Lorentzians (Table 10). As presented in Figure 3 right, the distribution of the energies and profiles of the satellites is similar with those of the Cu $K\beta_{1,3}$ diagram lines [1]. To our knowledge, it is the first time the energy positions and FWHM of the Ni $K\beta_1$ and $K\beta_5$ lines are obtained from a Lorentzian fitting analysis.

The measurement of the whole range of the $K\alpha$ and $K\beta$ lines was performed with the same setup with a 120 seconds accumulation time per energy point and with $0.01°$ step (see Table 7 3^{rd} line). The spectral lines were analyzed in the same way as previously. The ratio $K\beta_{1,3}/K\alpha_{1,2}$ was derived and found at $0.128(13)$ and is presented with other results in Table 6.

6 Conclusion

This work employed a multi-experimental approach to measure the complete set of atomic fundamental parameters of importance for X-ray spectrometry. This includes the mass attenuation coefficitents, the K-shell fluorescence yield, the $K\beta/K\alpha$ line ratio as well as relevant line energies, widths and relative intensities.

The mass attenuation coefficients are the basis of a lot of experimental X-ray measurements. Our

new experimental values should enable higher accuracy in any experimental work depending on them, as we performed high resolution measurements close to the transition edges and derived relative standard uncertainties close to 1% or even better. A comparison with existing tables has shown that EPDL97 and XCOM were the most reliable.

The K fluorescence yield was determined to be 0.410(14) which is close to the often used Krause value but with a reduced and reliable uncertainty. This is also a great benefit, as the Krause value was only provided with an extimated uncertainty.

The $K\beta/K\alpha$ and $K\beta_{1,3}/K\alpha_{1,2}$ intensity ratios were derived from three independent measurements using different experimental setups. The obtained values were found to be in excellent agreement within the experimental uncertainties. Theoretical predictions of Scofield [39] and Polasik [40] as well as the semi-empirical values from Schönfeld and Janssen [37] are consistent or nearly consistent with the present data. Tabulated values of Elam [33] and CXRO [34], however, are discrepant.

In addition, the contributions of the different satellites to the main diagram lines were distinguished by the double-crystal spectrometer and their relative importance were measured. As the energy resolution of the double-crystal spectrometer used in UNIKY is extremely high (1.45×10^{-5} at the nickel $K\beta_1$ line energy), fine structures as in Cu $K\beta_{1,3}$ spectra, were confirmed for the first time in Ni $K\beta_{1,3}$ lines. Moreover, the line energies, FWHM, [KM] contributions and asymmetry index in Ni $K\alpha_{1,2}$ spectra were reconfirmed using this spectrometer. The reported FWHM of all the lines were found to be in excellent agreement with tabulated values which is of prime interest for spectrometry purposes. In a near future the observed spin doublet of the $K\beta$ line will be discussed using theoretical calculation.

In conjunction with the other results, which have been and are to be determined within the framework of this collaboration and the International Fundamental Parameter Initiative, these results will eventually allow for the compilation of a new database for atomic fundamental parameters. However, at the present stage only very few chemical elements and not all relevant parameters could be redetermined with reliable uncertainty budgets. A continuation of this work and also the implementation of theoretical calculations and theoretically profound interpolations are in the scope of future works in order to be able to provide a new and more reliable database for these fundamental parameters.

Acknowledgments

The authors acknowledge the financial support for the determination of the FP data by the REXDAB collaboration that was initiated within the International Fundamental Parameter Initiative.

References

[1] M. Deutsch, G. Hölzer, J. Hartwig, J. Wolf, M. Fritsch, and E. Förster, "$K\alpha$ and $K\beta$ x-ray emission spectra of copper," *Physical Review A*, vol. 51, p. 283, 1995.

[2] Y. Ito, T. Tochio, H. Ohashi, M. Yamashita, S. Fukushima, M. Polasik, K. Słabkowska, . Syrocki, E. Szymańska, J. Rzadkiewicz, P. Indelicato, J. P. Marques, M. C. Martins, J. P. Santos, and F. Parente, "$K\alpha_{1,2}$ x-ray linewidths, asymmetry indices, and [KM] shake probabilities in elements Ca to Ge and comparison with theory for Ca, Ti, and Ge," *Physical Review A*, vol. 94, p. 042506, 2016.

[3] R. D. Deslattes, E. G. Kessler, P. Indelicato, L. de Billy, E. Lindroth, and J. Anton, "X-ray transition energies: new approach to a comprehensive evaluation," *Reviews of Modern Physics*, vol. 75, no. 1, pp. 35–99, 2003.

[4] J. L. Glover, C. T. Chantler, Z. Barnea, N. A. Rae, C. Q. Tran, D. C. Creagh, D. Paterson, and B. B. Dhal, "Measurement of the x-ray mass-attenuation coefficient and imaginary component of the form factor of copper," *Physical Review A*, vol. 78, p. 052902, 2008.

[5] C. T. Chantler, J. Lowe, and I. P. Grant, "High-accuracy reconstruction of titanium x-ray emission spectra, including relative intensities, asymmetry and satellites, and ab initio determination of shake magnitudes for transition metals," *Journal of Physics B*, vol. 46, no. 1, p. 015002, 2013.

[6] J. M. Sampaio, T. I. Madeira, J. P. Marques, F. Parente, A. M. Costa, P. Indelicato, J. P. Santos, M.-C. Lépy, and Y. Ménesguen, "Approaches for theoretical and experimental determinations of K-shell decay rates and fluorescence yields in Ge," *Physical Review A*, vol. 89, p. 012512, 2014.

[7] Y. Ménesguen, M. Gerlach, B. Pollakowski, R. Unterumsberger, M. Haschke, B. Beckhoff, and M.-C. Lépy, "High accuracy experimental determination of copper and zinc mass attenuation coefficients in the 100 eV to 30 keV photon energy range," *Metrologia*, vol. 53, pp. 7–17, 2016.

[8] B. Beckhoff, "Reference-free X-ray spectrometry based on metrology using synchrotron radiation," *Journal of Analytical Atomic Spectrometry*, vol. 23, p. 845, 2008.

[9] J.-Cl. Dousse and J. Hoszowska, "L- and M-shell electron shake process following 1s photoionization in argon and krypton," *Phys. Rev. A*, vol. 56, p. 4517, 1997.

[10] J. Hoszowska, J.-Cl. Dousse, W. Cao, K. Kennane, Y. Kayser, and M. Szlachetko, "Double K-shell photoionization and hypersatellite x-ray transitions of $12 \leq Z \leq 23$ atoms," *Phys*, vol. 82, p. 063408, 2010.

[11] W. Cao, M. Kavčič, J.-Cl. Dousse, M. Berset, K. Bučar, M. Budnar, K. Fennane, J. Hoszowska, Y.-P. Maillard, J. Szlachetko, M. Szlachetko, and M. Žitnik, "High-resolution KMM radiative Auger x-ray emission spectra of calcium induced by synchrotron radiation," *Phys. Rev. A*, vol. 83, p. 042513, 2011.

[12] B. Nordfors, "The statistical errors in X-ray absorption measurements," *Arkiv Fysik*, vol. 18, pp. 37–47, 1960.

[13] F. Senf, U. Flechsig, F. Eggenstein, W. Gudat, R. Klein, H. Rabus, and G. Ulm, "A plane-grating monochromator beamline for the PTB undulators at BESSY II," *Journal of Synchrotron Radiation*, vol. 5, pp. 780–782, 1998.

[14] F. Schölze, B. Beckhoff, G. Brandt, F. Fliegauf, A. Gottwald, R. Klein, B. Meyer, D. Rost, U. Schwarz, R. Thornagel, J. Tümmler, K. Vogel, J. Weser, and Ulm, "High-accuracy EUV metrology of PTB using synchrotron radiation," *Proceedings of SPIE*, vol. 4344, pp. 402–413, 2001.

[15] M. Krumrey and G. Ulm, "High-accuracy detector calibration at the PTB four-crystal monochromator beamline," *Nuclear Instruments & Methods in Physics Research, Section A: Accelerators, Spectrometers, Detectors, and Associated Equipment*, vol. 467-468, pp. 1175–1178, 2001.

[16] Goodfellow Cambridge Limited (GB). Consultation date: 2015. [Online]. Available: http://www.goodfellow.com/home.aspx

[17] JCGM, *Evaluation of measurement data - Guide to the expression of uncertainty in measurement*. BIPM, 2008, consultation date: 2015. [Online]. Available: http://www.bipm.org/fr/publications/guides/gum.html

[18] Y. Ménesguen and M.-C. Lépy, "Mass attenuation coefficients in the range $3.8 \leq E \leq 11$ kev, K fluorescence yield and K_β/K_α relative X-ray emission rate for Ti, V, Fe, Co, Ni, Cu, and Zn measured with a tunable monochromatic X-ray source," *Nuclear Instruments & Methods In Physics Research B*, vol. 268, no. 16, pp. 2477–2486, 2010.

[19] B. L. Henke, E. M. Gullikson, and J. C. Davis, "X-ray interactions: photoabsorption, scattering, transmission, and reflection at E = 50-30000 eV, Z = 1-92," *Atomic Data and Nuclear Data Tables*, vol. 54, no. 2, pp. 181–342, 1993.

[20] C. T. Chantler, "Theoretical form factor, attenuation and scattering tabulations for Z=1-92 from E=1-10 eV to E=0.4-1.0 MeV," *Journal of Physical and Chemical Reference Data*, vol. 24, pp. 71–643, 1995.

[21] D. E. Cullen, J. H. Hubbell, and L. Kissel, "Epdl97: the Evaluated Photon Data Library, '97 Version"," *UCRL-50400*, vol. 6, no. 5, 1997, consultation date: 2015. [Online]. Available: http://www.llnl.gov/cullen1/document/epdl97/epdl97.pdf

[22] M. J. Berger, J. H. Hubbell, S. M. Seltzer, J. Chang, J. S. Coursey, R. Sukumar, and D. S. Zucker, *XCOM: Photon Cross Section Database (version 3.1)*, National Institute of Standards and Technology Std., 2010, consultation date: 2015. [Online]. Available: http://physics.nist.gov/xcom

[23] M. O. Krause, C. W. Nestor, C. J. Sparks, and E. Ricci, "X-ray fluorescence cross sections for k and l X-rays of the elements," *Oak Ridge National Laboratory*, vol. 5399, 1978.

[24] M. Kolbe, P. Hönicke, M. Müller, and B. Beckhoff, "L-subshell fluorescence yields and coster-kronig transition probabilities with a reliable uncertainty budget for selected high- and medium-z elements," *Physical Review A*, vol. 86, p. 042512, 2012.

[25] P. Hönicke, M. Kolbe, M. Krumrey, R. Unterumsberger, and B. Beckhoff, "Experimental determination of the oxygen K-shell fluorescence yield using thin SiO_2 and Al_2O_3 foils," *Spectrochim. Acta B (2016) 124, 94-98*, vol. 124, pp. 94–98, 2016.

[26] M. O. Krause, "Atomic Radiative and Radiationless Yields for K and L Shells," *Journal of Physical and Chemical Reference Data*, vol. 8, no. 2, pp. 307–328, 1979.

[27] M. Kolbe and P. Hönicke, "Fundamental parameters of Zr and Ti for a reliable quantitative X-ray fluorescence analysis," *X-ray Spectrometry*, vol. 44, no. 4, pp. 217–220, 2015.

[28] J. Hoszowska, J.-Cl. Dousse, J. Kern, and C. Rhême, "High-resolution von Hamos crystal X-ray spectrometer," *Nuclear Instruments & Methods in Physics Research: Section A*, vol. 376, pp. 129–138, 1996.

[29] J. Szlachetko, M. Nachtegaal, E. de Boni, M. Willimann, O. Safonova, J. Sa, G. Smolentsev, M. Szlachetko, J. A. van Bokhoven, J.-Cl. Dousse, J. Hoszowska, Y. Kayser, P. Jagodzinski, A. Bergamaschi, B. Schmitt, C. David, and A. Lücke, "A von Hamos x-ray spectrometer based on a segmented-type diffraction crystal for single-shot x-ray emission spectroscopy and time-resolved resonant inelastic x-ray scattering studies," *Review of Scientific Instruments*, vol. 83, p. 103105, 2012.

[30] J. Szlachetko, J.-Cl. Dousse, J. Hoszowska, M. Berset, W. Cao, M. Szlachetko, and M. Kavcic, "Relative detection efficiency of back- and front-illuminated charge-coupled device cameras for x-rays between 1 keV and 18 keV," *Review of Scientific Instruments*, vol. 78, p. 093102, 2007.

[31] *Status of XOP: an x-ray optics software tookit*, vol. 5536. SPIE, August 2004.

[32] L. V. Azaroff, *Elements of X-ray Crystallography*. McGraw-Hill Inc, 1968.

[33] W. T. Elam, B. D. Ravel, and J. R. Sieber, "A new atomic database for X-ray spectroscopic calculations," *Radiation Physics and Chemistry*, vol. 63, pp. 121–128, 2002.

[34] A. Thompson, D. Attwood, E. Gullikson, M. Howells, K.-J. Kim, J. Kirz, K. J., I. Lindau, Y. Liu, P. Pianetta, A. Robinson, J. Scofield, J.and Underwood, and G. Williams, *X-ray data booklet*. Lawrence Berkeley National Laboratory, University of california, 2009.

[35] G. Hölzer, M. Fritsch, M. Deutsch, J. Härtwig, and E. Förster, "$K\alpha_{1,2}$ and $K\beta_{1,3}$ x-ray emission lines of the 3d transition metals," *Physical Review A*, vol. 56, p. 4554, 1997.

[36] B. Ertugral, G. Apaydin, U. Cevik, M. Ertugrul, and A. I. Kobya, "$K\beta/K\alpha$ X-ray intensity ratios for elements in the range $16 \leq E \leq Z \leq 92$ excited by 5.9, 59.5 and 123.6 kev photons," *Radiation Physics and chemistry*, vol. 76, pp. 15–22, 2007.

[37] E. Schönfeld and H. Janssen, "Evaluation of atomic shell data," *Nuclear Instruments & Methods In Physics Research A*, vol. 369, pp. 527–533, 1996.

[38] J. H. Scofield, "Relativistic Hartree-Slater values for K and L X-ray emission rates," *Atomic Data and Nuclear Data Tables*, vol. 14, pp. 121–137, 1974.

[39] ——, "Exchange corrections of K x-ray emission rates," *Phys. Rev. A*, vol. 9, no. 3, pp. 1041–1049, 1974.

[40] M. Polasik, "Influence of changes in the valence electronic configuration on the $K\beta$-to-$K\alpha$ x-ray intensity ratios of the 3d transition metals," *Physical Review A*, vol. 58, p. 1840, 1998.

[41] H. Berger, "Study of the $K\alpha$ emission spectrum of copper," *X-ray spectrometry*, vol. 15, no. 4, pp. 241–243, 1986.

[42] Y. Ito, T. Tochio, and A. M. Oohashi, H.and Vlaicu, "Contribution of the [1s3d] shake process to $K\alpha_{1,2}$ spectra in 3d elements," *Radiation Physics and Chemistry*, vol. 75, p. 1534, 2006.

[43] 16th International Conference on Physics of Highly Charged Ions, Ed., *The $K\alpha_{1,2}$ linewidths for 3D transition metals*, 2012.

[44] M. O. Krause and J. H. Oliver, "Natural Widths of Atomic K and L level, K_α X-Ray Lines and Several KLL Auger Lines," *Journal of Physical and Chemical Reference Data*, vol. 8, no. 2, pp. 329–338, 1979.

[45] C. T. Chantler, M. N. Kinnane, C.-H. Su, and J. A. Kimpton, "Characterization of $K\alpha$ spectral profiles for vanadium, component redetermination for scandium, titanium, chromium, and manganese, and development of satellite structure for Z=21 to Z=25," *Physical Review A*, vol. 73, p. 012508, 2006.

[46] D. F. Anagnostopoulos, R. Sharon, D. Gotta, and M. Deutsch, "$K\alpha$ and $K\beta$ x-ray emission spectra of metallic scandium," *Physical Review A*, vol. 60, p. 2018, 1999.

[47] J. A. Lowe, C. T. Chantler, and I. P. Grant, "Ab initio determination of satellite intensities in transition-metal photoemission spectroscopy using a multiconfiguration framework," *Physical Review A*, vol. 83, p. 060501(R), 2011.

[48] T. Tochio, Y. Ito, and K. Omote, "Broadening of the x-ray emission line due to the instrumental function of the double-crystal spectrometer," *Physical Review A*, vol. 65, p. 042502, 2002.

[49] J. A. Bearden, "X-Ray Wavelengths," *Review of Modern Physics*, vol. 39, p. 78, 1967.

[50] J. L. Campbell and T. Papp, "Widths of atomic K-N7 levels," *Atomic Data and Nuclear Data Tables*, vol. 77, pp. 1–56, 2001.